

# A Generic Multi-Criteria Design Approach Toward High Power Density and Fault-Tolerant Low-Speed PMSM for Pod Applications

Ioannis D. Chasiotis, *Student Member, IEEE*, and Yannis L. Karnavas<sup>1</sup>, *Member, IEEE*

**Abstract**—Pod propulsion systems are widely used, since they exhibit high efficiency and reliability, especially when they are combined with permanent magnet synchronous motors (PMSMs). Except from high efficiency, high power density and increased fault-tolerance capability are also the main requirements for a motor in order to be used in such an application. Generally, PMSMs present high power density in high-speed operation. However, in low-speed applications, the achievement of increased power density is not an easy task. Moreover, PMSMs with surface-mounted magnets are characterized by low winding self-inductance which limits the fault-tolerance capability. Thus, this paper presents an effective generic multicriteria PMSM design approach and proposes a global selection strategy for both the slots/poles combination and the motor's airgap diameter to axial length ratio aiming to enhance the two aforementioned characteristics. At the same time, numerous practical and physical constraints have been thoroughly described and taken into account in the proposed process. These constraints are not adequately presented in the relative literature. The derived topologies are validated through finite element method analysis and several important quantities are calculated and used as comparison metrics. Finally, useful conclusions are extracted that could be of great help for designers and manufacturers of pod propulsion systems.

**Index Terms**—Fault tolerance capability, finite-element analysis, high efficiency, high power density, multi-criteria design, permanent magnet synchronous motor (PMSM), pod propulsion system.

## I. INTRODUCTION

SINCE the early 20th century electrical machines have been employed in cruise ships, ferries, yachts, battle ships, icebreakers, shuttle tankers, special purpose and research vessels (e.g., for oceanographic explorations), and so on [1]. They have been used so far either as parts of ship's auxiliary systems or as the prime mover of the propeller. Nowadays, integrated electric ships are becoming common throughout the commercial marine industry due to the rapid development of power electronics technology and the advancements in machine design [2]. This prospect leads to important benefits considering the fuel consumption reduction, while simultaneously it offers significant advantages in efficiency, performance

at low speed, maneuverability, safety, and plant flexibility compared to the conventional diesel-mechanical systems [3].

The last trend in electric ship propulsion is the “podded” propulsor, in which the prime mover is located outside of the ship's hull and mounted in an Azimuthing pod below the ship's stern, as shown in Fig. 1. The pod system eliminates the need of a gearbox and allows the propeller to be directly mounted to the electric motor system. The replacement of mechanical coupling between them: 1) contributes to considerable savings in space and power consumption; 2) increases the system's efficiency and reliability; 3) improves the ship's handling during the navigation in swallow water and embarkation/disembarkation phases; and 4) reduces the maintenance cost [4]. Furthermore, it provides a high comfort class rating to the ship's crew and passengers due to the limitation of vibration and noise. Thus, the pod propulsion system can be considered as the most promising technology for small- and medium-size passenger vessels whose maximum speed is below 21 knots.

A motor, which is to be used in such a system, has to exhibit high efficiency and power factor due to the limited power source capability, acceptable temperature behavior, low cogging torque, and torque ripple. At the same time, it has to present increased power and torque density. Regarding the last mentioned features various structures, such as induction motors (IMs) [5], permanent magnet synchronous motors (PMSMs) [6], high-temperature superconducting motors (HTSMs) [7], and acyclic homopolar motors [8] have been already investigated and compared to each other in recent studies. Homopolar motors are low-voltage and high-current machines, and thus, they cannot easily be used in such an application. An HTSM can exhibit a power density almost twice than the corresponding one of an IM and over 25% higher than the one achieved by a PMSM [9]. However, the cost of the superconducting materials for the 2G HTSM technology is currently prohibitive and the wire supply chain cannot meet the commercial time frame. As the PMSMs have great advantages over IMs, it seems that they are the most realistic and suitable choice for a pod propulsion system.

In the case of PMSM technology, radial flux (with surface [10] and interior [11] magnets), axial [12], and transverse flux [13] topologies have been so far examined. Axial flux machines are short in length and require a quite larger diameter in order to develop significant torque. The transverse

Manuscript received July 31, 2018; revised December 10, 2018; accepted January 11, 2019. Date of publication January 24, 2019; date of current version June 19, 2019. (Corresponding author: Yannis L. Karnavas.)

The authors are with the Electrical Machines Laboratory, Department of Electrical and Computer Engineering, Democritus University of Thrace, 671 00 Xanthi, Greece (e-mail: ichasiotis@ee.duth.gr; karnavas@ee.duth.gr).

Digital Object Identifier 10.1109/TTE.2019.2894995

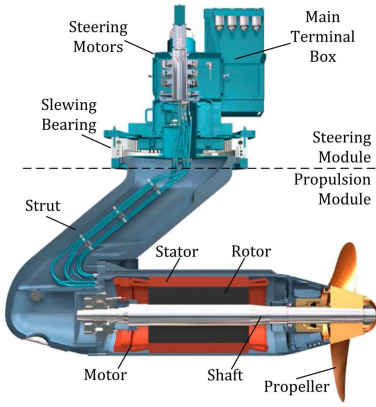


Fig. 1. Basic components of a pod propulsion system.

flux configuration is quite promising from the aspect of torque density, but presents low power factor and increased manufacturing complexity. Several research efforts (see [14]) have so far succeeded to fulfill the majority of the aforementioned requirements when the radial flux topologies have been used. These efforts though were conducted with respect to topologies with interior permanent magnets mainly, so the corresponding ones with surface magnets have to be studied more. In addition, relevant works (see [15]) are focusing on the optimization of motor's configuration in order to guarantee low back electromotive force harmonic content, high overall performance, and non-saturable operation without trying to minimize the motor's mass and increase fault-tolerance capability, which are essential characteristics from an industrial perspective.

The achievement of high power density usually coincides with high-speed operation and multiphase systems. However, the maximum speed of the vessels with a direct-drive propulsion system is usually in the range of 100–500 rpm and 650–1800 rpm for low- and high-speed ships, respectively. Moreover, a multiphase supply system is not a common practice in commercial electric ships [16]. Conventional low-speed PMSMs for traction applications can reach a power density of 1.5 kW/kg when they are combined with large poles number. This relatively high power density is achievable when the motor can obtain a larger diameter compared to its length [17]. This requirement cannot actually be met in a typical pod structure, as the one shown in Fig. 1. A review in the relevant technical literature of the major pod system manufacturers, such as ABB, Rolls Royce, Siemens-Schottel, Wartsila SAM Electronics, GE Power Conversion, and General Dynamic Electric Boat, confirmed the low power density ratings of the already installed motors. Through the extended literature review, the authors collected data about the power density ratings of the above-mentioned motors. The derived results are shown in Fig. 2. It is clear enough that there is a strong “connection” among the motor's power density, its output power, its rotation speed, and the level of the supply voltage.

On the basis of the above, this paper presents a practical effective and generic multicriteria design approach for PMSMs

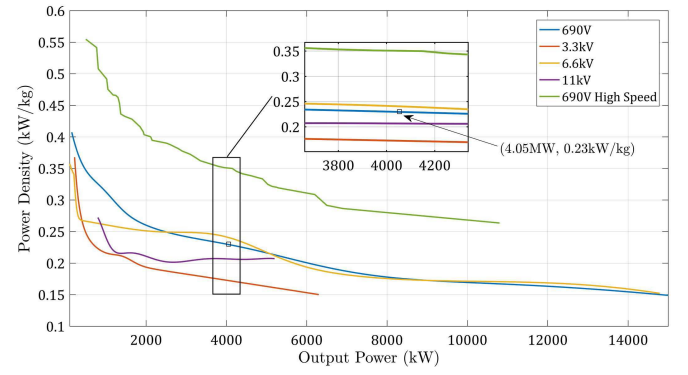


Fig. 2. Maximum power density presented by motors which are already installed in commercial electric ships with a direct-drive propulsion system.

that are going to be used in low-speed ferries. The overall proposed procedure aims to enhance motors' fault-tolerance capability and at the same time increase their power density beyond the ratings that are provided in Fig. 2. To meet these goals, the developed methodology incorporates the followings: 1) the estimation of the ship's propeller performance; 2) the determination of the propulsion motor characteristics according to the propeller's specifications; 3) the choice of the proper winding type; 4) the deployment and implementation of a selection strategy for the poles/slots combinations; 5) the development of numerous PMSM topologies that satisfy the set requirements; 6) the investigation of the effect of motor's airgap diameter to its axial length ratio on several important quantities that have been used as comparison metrics; 7) the further assessment of derived configurations; and 8) the proposal of some elimination criteria in order to conclude to topologies that exhibit a more “balanced” performance. In addition, in order to guarantee that the topologies will be acceptable from an industrial perspective various physical and practical constraints have been taken into account during the design process. These constraints are not clarified and incorporated in the already published scientific works, and thus, they are thoroughly presented and discussed here. A software tool, developed by the authors, permitted the conduction of the aforementioned investigations. Also, finite element method (FEM) analysis was conducted in order to validate the motor's performance. Finally, the results obtained at each step of this methodology are discussed and some directions are provided that could be considered useful for engineers, designers, and pod propulsion system manufacturers.

## II. PROPULSION SYSTEM SPECIFICATIONS

### A. Propeller Design Procedure

The vessel's speed and size are the basic criteria for the selection of a pod propulsion motor. The estimation of motor's characteristics comes across with the determination of the propeller's geometrical parameters and the analysis of its performance. The propeller's power ( $P_B$ ) in kilowatt and its torque ( $Q_B$ ) in kNm are obtained from (1) and (2), where  $k_Q$  is the torque coefficient,  $\rho$  is the water density in kg/m<sup>3</sup>,  $n$  is the rotational speed in rps, and  $D$  is the propeller's

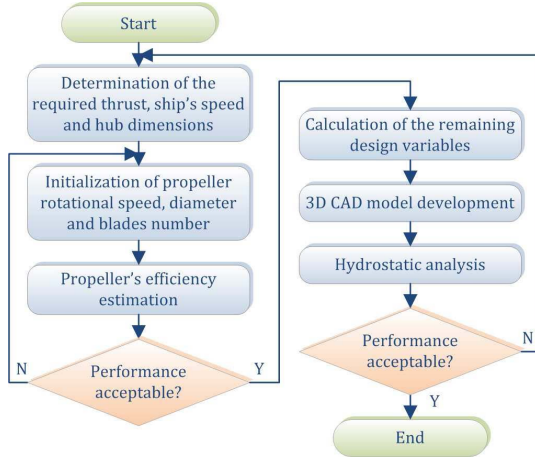


Fig. 3. Propeller's design and optimization procedure flowchart.

diameter in meter. Since a direct-drive propulsion system is examined here, the quantities calculated by these equations are equal to the motor's output torque and power, respectively. The design process of a fixed-pitch propeller includes the specification of several parameters, such as the blades number, its diameter, and rotational speed, which have to be carefully selected. For instance, the small number of blades benefits the efficiency. On the other hand, propellers with only 2 or 3 blades are not usually suitable for medium passenger ferries (as in our case), since they are subjected to heavy loads. Moreover, for low-speed vessels (i.e., under 35 knots), it is a common practice to reduce the rotational speed and increase the propeller's diameter in order to obtain higher torque for a given power plant [18]. The diameter has great effect on the power that a propeller can absorb and the thrust that is available for propulsion. Furthermore, this geometrical parameter imposes several design constraints related with the pod structure and the motor's dimensions. These constraints are going to be discussed in Section IV.

$$Q_B = k_Q \rho n^2 D^5 \quad (1)$$

$$P_B = 2\pi n Q_B \quad (2)$$

Taking the above into consideration, the propeller topology was designed and optimized by following the procedure presented in Fig. 3. The first step involves the determination of the vessel's speed, the required thrust, and the dimension of the propeller's hub. For the examined here case, the ship's speed has been set equal to 10 m/sec, while the required thrust was assumed to be equal to 300 kN. The hub's diameter was selected to be as small as possible in order to obtain the maximum thrust. However, there is a tradeoff between the hub's size and its mechanical strength. A too small hub will not be able to guarantee an overall robust structure. At this initial point, the specific parameter has been considered equal to 0.8 m. Its value may be needed to be reestimated later based on the preliminary results.

Afterward, the conduction of a parametric analysis follows aiming to specify the main geometrical features. At each step of this analysis, the propeller's efficiency and its hydrodynamic

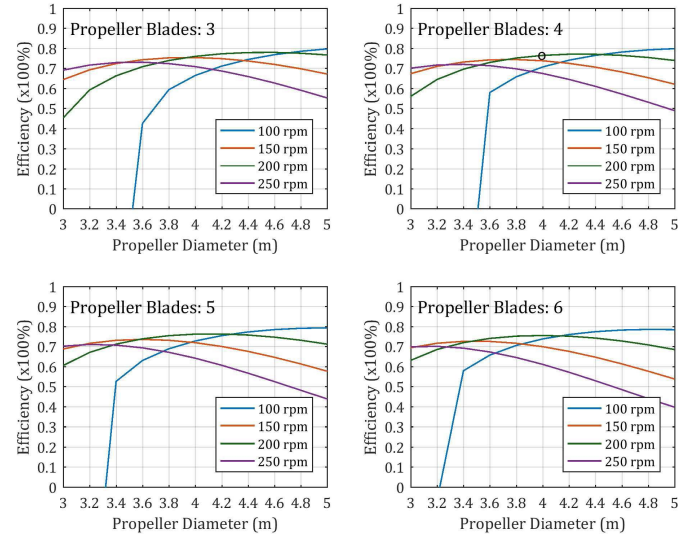


Fig. 4. Propeller's efficiency variation as a function of its rotational speed, diameter, and number of blades.

curve were determined by using OpenProp, an open-source software that incorporates a unified motor lifting line model based on the "numerical vortex lattice theory." The reader can refer to [19] in order to find more information about this model. The variation of the propeller's efficiency as a function of its diameter, speed, and blades number is shown in Fig. 4. By observing the derived results, the followings can be concluded: 1) the rotational speed of 250 rpm leads to the lowest efficiency for each one of the examined cases, and thus, it can be excluded from the next steps of the followed procedure; 2) the selection of 100 rpm for the propeller's speed is preferable only when its diameter is larger than 4.4 m; and 3) the maximum achievable efficiency when five or six blades are used is very close to the corresponding one obtained in the case of three and four blades and, consequently, these two cases (i.e., five and six blades) could also be excluded.

Next, for each one of the remaining cases (i.e., three different speeds with three or four blades), the selected propeller's diameters were those that guaranteed efficiency close to the maximum one achieved through the parametric investigation. Then, for a given diameter, the blade's design variables (e.g., the blade chord, the leading edge, and the trailing edge) were calculated through an optimization process which was terminated when the propeller's overall high performance was achieved. After this step, the 3-D model for each one of the derived propeller configurations was created by using a CAD software, and finally, hydrostatic analysis was performed for all of them. The above-mentioned approach revealed that the propellers with three blades were subjected to a large amount of hydrostatic pressure and, thus, they had also to be rejected. The final choice was a propeller with four blades, 200-rpm rotational speed, and a diameter of 4 m. The hydrodynamic curves of the final propeller topology are shown in Fig. 5(a). In these curves, the thrust coefficient ( $K_T$ ), the torque coefficient ( $10K_Q$ ), and the propeller's efficiency ( $Eff$ ) are represented as a function of the advance



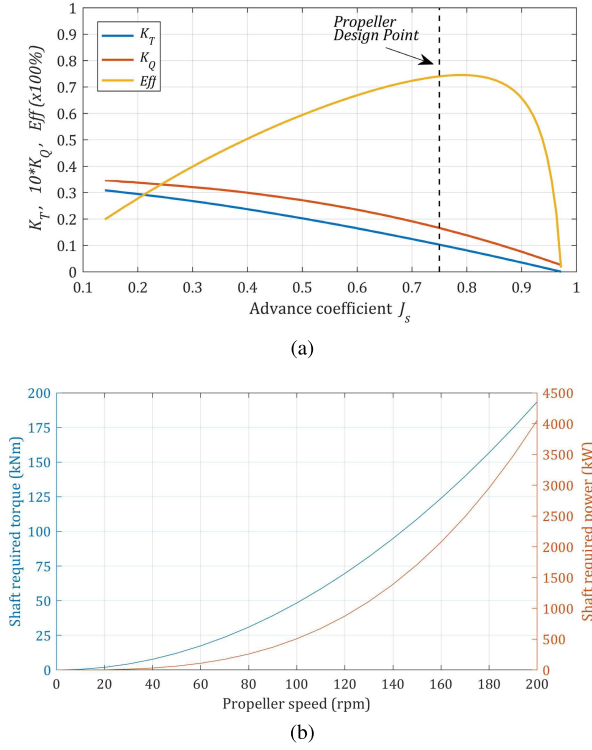


Fig. 5. (a) Hydrodynamic curve of the selected propeller topology. (b) Requirements of propeller's shaft torque and power versus speed.

coefficient ( $J_s$ ). At its nominal operating point (marked on the specific curve), the propeller exhibits an efficiency equal to 76% which is quite satisfactory. Furthermore, the propeller's shaft torque and power requirements versus speed are depicted in Fig. 5(b). A 3-D view of the final topology is depicted in Fig. 6. In the same figure, a detailed view of one blade is also given.

### B. POD Motor Characteristics

From Fig. 5(b), it is obvious that the maximum power and torque are delivered to the propeller when it reaches its maximum speed. Thus, the design approach of a pod propulsion motor does not need to guarantee a wide constant power speed range (CPSR). In this case, the CPSR requirement is nearly 1:1, which means that the motor's field weakening operation is almost unnecessary according to [20]. Consequently, the main advantage (i.e., the enhanced field-weakening operation) of the PMSMs with inner permanent magnets is not of great importance. For this reason, the perspective of PMSMs with surface-mounted magnets seems to be very attractive and should be examined in detail. For the PMSM under investigation here, its rated speed has been considered equal to the maximum propeller's speed, while the required motor's output power has been estimated and set equal to 4.054 MW. A torque of 193.58 kNm has to be delivered to the propeller's shaft at a speed of 200 rpm. The motor has to fulfill the torque and power requirements according to the load characteristics shown in Fig. 5(b) through the proper adjustment of the frequency and the applied voltage level. The additional amount

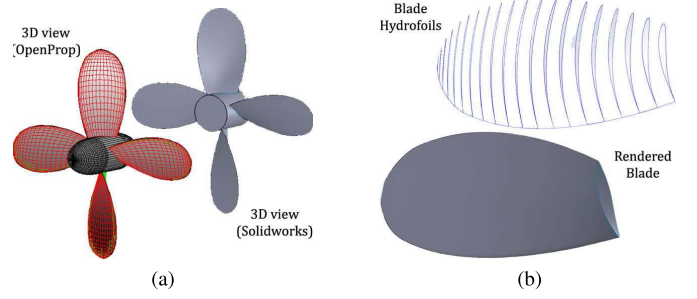


Fig. 6. 3-D view of (a) final propeller's topology and (b) one propeller's blade.

of torque that the motor may provide to the propeller will be used to meet the vessel's speed up requirements.

## III. ENHANCEMENT OF FAULT-TOLERANCE CAPABILITY

### A. Winding-Type Selection

The pod propulsion motors provide a large amount of torque to the propeller's shaft absorbing high currents for long time periods, which can lead to high failure rates. Thus, an increased fault-tolerance capability is required. Both motor's control and design techniques can contribute to this direction. For instance, an electrical separation among phases can be achieved when each one is fed by a different inverter. However, the above is not commonly used in the commercial electrical ships [21]. On the other hand, the proper design choices can benefit this characteristic. Among the most important ones is the selection of the stator winding configuration. Specifically, a phase to phase fault can be prevented when each slot contains only one coil side. The physical separation is also possible when fractional slots PMSMs with concentrated nonoverlapped windings are used. This winding type results in high self-inductance and low mutual inductance among phases, which can become even equal to zero when a single layer winding is preferred and the proper poles/slot combinations are chosen. A high self-inductance limits the short-circuit current to a given threshold, while simultaneously the magnetic isolation among phases prevents its further increment. Another beneficial feature of the specific winding type is that enables the motor to be slit up in several identical parts. The modularity provides important manufacturing advantages and reduces the likelihood of an interphase fault. Moreover, the motor's maintenance is much easier and less time-consuming, which is quite attractive from commercial perspective [22].

### B. Poles/Slots Combination Selection Strategy

Even fractional-slot PMSMs can be subjected to high vibration and extensive radial magnetic forces if the proper poles/slots combination has not been chosen. In the case of pod propulsion motors, there are strict limits on noise, vibration, and other parasitic effects (e.g., torque ripple, cogging torque, and so on) in order to ensure that high-class comfort ratings will be provided to the vessel's crew and passengers. Various methodologies have been so far proposed aiming to help PMSM designers to make the appropriate decision. Among

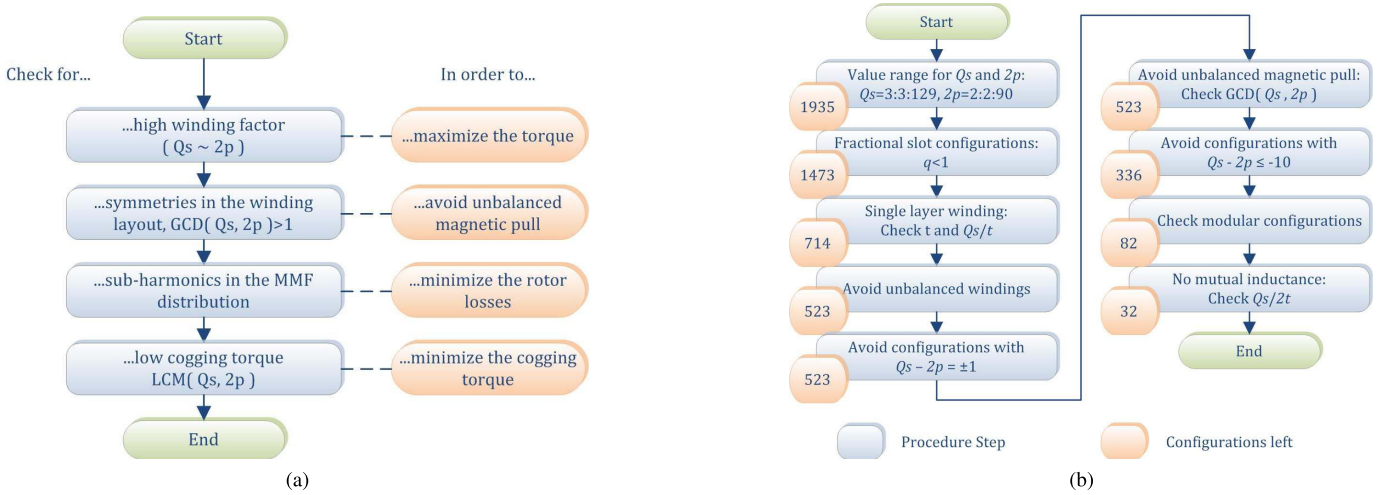


Fig. 7. Poles/slots combination selection methodologies. (a) One presented in [23]. (b) New one proposed here.

the most commonly used is the one presented in [23] and illustrated in Fig. 7(a). According to the specific approach, the selection of poles ( $2p$ ) and slots ( $Q_s$ ) starts by searching for combinations with high fundamental winding factor ( $k_w$ ). A high  $k_w$  maximizes the output torque and benefits the power density, as less turns per phase and, thus, less copper mass are required. At the next steps, the designer must avoid the combinations that do not present symmetry, lead to unbalanced magnetic pull, excessive rotor losses, and cogging torque. Regarding to the last phenomenon, the least common multiple (LCM) of  $2p$  and  $Q_s$  is an adequate indicator of its peak amplitude.

Nevertheless, the specific methodology exhibits some clear cons: 1) the search space for  $2p$  and  $Q_s$  is quite wide; 2) the calculation of  $k_w$  for each one of all the possible combinations is a very demanding and time-consuming procedure; 3) all the parasitic effects will not be eliminated even after the employment of the relative constraints (see Step 2 of this methodology); and 4) no one of the features that were described in Section III.A (i.e., fractional-slot topology, modularity, increased fault-tolerance capability, and so on) and are of great importance for this application can be met. For this reason and by taking into account the pod systems' requirements and the industrial practices, the authors propose here a simple but effective selection strategy, which is presented in Fig. 7(b) in a flowchart form. In the same figure, the number of the candidate solutions that has remained after the employment of the corresponding criteria is also given for each one of the applied steps. The selection strategy process is described in steps as follows.

**Step 1:** The search space for  $2p$  and  $Q_s$  has to be determined. Since it is not clear so far which combinations are more suitable for the examined here PMSM, authors decided to vary  $2p$  from 2 to 90 with a step of 2 and  $Q_s$  from 3 to 129 with a step of 3.

**Step 2:** For fractional-slot topologies, the number of slots per pole per phase ( $q$ ) must be less than 1,

i.e.,  $q < 1$ . The above quantity is defined as  $q = Q_s/(m2p)$ , where  $m$  is the number of phases. In our case  $m = 3$ .

**Step 3:** A single layer configuration is always possible when the machine periodicity  $t = GCD(Q_s, p)$  is an even number ( $p$ : pole pairs). If  $t$  is odd, a single layer can be implemented only when  $Q_s/t$  is even [24].

**Step 4:** The combinations that give an unbalanced three-phase winding are excluded next. This happens when the quantity  $Q_s/(mGCD(Q_s, 2p))$  is not an integer.

**Step 5:** The combinations for which  $Q_s$  and  $2p$  are related by  $Q_s - 2p = \pm 1$  should also be rejected, as they inherently present unbalanced magnetic pull and consequently asymmetric magnetic loading, noise, and vibration.

**Step 6:** For the same reasons as those mentioned in Step 5, combinations with  $GCD(Q_s, 2p) < 1$ , should also be excluded.

**Step 7:** The combinations with  $2p$  quite larger than  $Q_s$  should also be avoided, as high flux leakage is observed. In this paper, the eliminating criterion has been set to:  $Q_s - 2p \leq -10$ .

**Step 8:** Motor's modularity (i.e., split-up in parts with the same coils number) is possible when the quantity  $Q_s/(m|Q_s - 2p|)$  is integer [22].

**Step 9:** A zero mutual inductance among phases derives for a single layer winding when the quantity  $Q_s/2t$  is even.

By observing Fig. 7(b), it can be seen that only 32 poles/slots combinations fulfill all the requirements that have been previously described. Their number is equal to 1.65% and 6.11% of the possible cases that derived after the employment of Step 1 and Step 6, respectively. Thus, the research space for this problem can be significantly limited by following the proposed here methodology. Another important aspect is that these 32 combinations (presented in Table I)

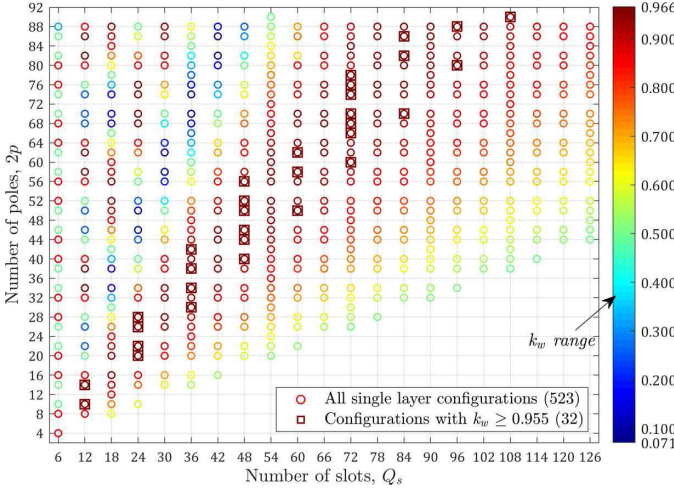


Fig. 8. Winding factor distribution for the remained combinations after the employment of: (a) Step 6 (523 cases) and (b) Step 9 (32 cases).

TABLE I  
SLOTS/POLES COMBINATIONS DERIVED THROUGH  
THE PROPOSED METHODOLOGY

Poles number ( $2p$ )	Slots number ( $Q_s$ )	Winding factor ( $k_w$ )
10, 14	12	0.966
20, 28	24	0.966
22, 26	24	0.958
30, 42	36	0.966
34, 38	36	0.956
40, 56	48	0.966
44, 52	48	0.958
46, 50	48	0.956
50	60	0.966
58, 62	60	0.955
60	72	0.966
66, 78	72	0.958
68, 76	72	0.956
70, 74	72	0.955
70	84	0.966
82, 86	84	0.955
80	96	0.966
88	96	0.958
90	108	0.966

exhibit high  $k_w$ . By incorporating the appropriate constraints, the combinations with a low  $k_w$  (shown in Fig. 8) have been eliminated without this feature being the basic priority in our case in contrast with the procedure presented in [23].

Consequently, the described, here, selection strategy has clear benefits in terms of completeness than any other similar methodology proposed so far in the literature. Moreover, it is quite easy for a designer to adopt the complete process or only partially, as each step is individually presented and explained.

#### IV. MULTICRITERIA PMSM DESIGN APPROACH

##### A. Problem Specifications and Constraints

The cross section of a typical PMSM topology with surface-mounted magnets is presented in Fig. 9(a), where its main geometrical characteristics are shown, while Fig. 9(b) provides a detailed view of the stator slot's parameters.

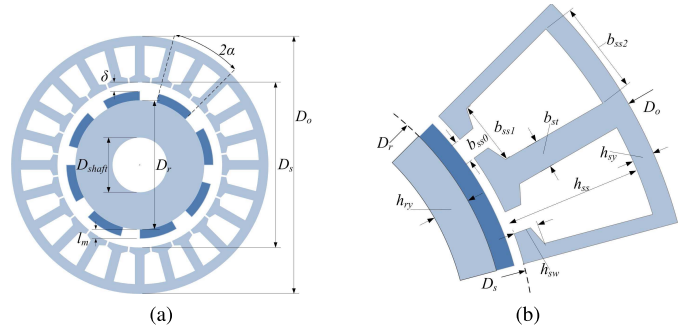


Fig. 9. General representation of a typical PMSM topology. (a) Cross-section view of the whole motor. (b) Detailed view of the stator slots.

Although the design procedure of PMSMs is a well-established knowledge, in the case of pod propulsion motors, a different approach is needed, since there is a large number of constraints which are imposed by the specific application. In addition, the current relevant literature lacks examples, in which the aforementioned constraints are thoroughly discussed. This paper aims to fill this gap by presenting and analyzing these constraints and also incorporating them in the proposed design process. The applied constraints are divided in five different categories, as they are related with performance, electrical, physical, mechanical, and magnetic characteristics. Regarding the first group, the PMSM must exhibit high efficiency (i.e., over 95%) according to the latest trends for motors with superpremium efficiency and the pod system manufacturers' demands. Furthermore, its power factor has to be at least equal to 0.95. The above features are quite important, as the propulsion motor has great effect on the ship's overall system performance; on the other hand, at the same time, there is limited power source capability.

Regarding to the electrical quantities, there are four mains connection voltage levels (i.e., 690 V, 3.3 kV, 6.6 kV, and 11 kV), which are usually used in the commercial electric ships. For small- and medium-size ferries, in which motors with output power in the range of 2.2–4.5 MW are placed, the most common one is that of 690 V. For the case study here, a typical inverter provides to the motor a line to line voltage in the range of 525–690 V. Moreover, a low frequency is preferable in order to keep in low levels the motor's core losses. Thus, the upper bound for this parameter has been set equal to 150 Hz. Furthermore, there is a limit for the maximum current that the motor can absorb by the inverter. In this paper, this limit has been set equal to 4.5 kA taking into account the performance characteristics of commercial inverters that are used to drive ship propulsion motors with a similar output power. Another important constraint concerns the winding's current density. It is a common practice for marine industry not to utilize a cooling arrangement when PMSMs with the aforementioned supply voltage are used. The motor is cooled directly by the seawater that surrounds the pod structure. A low current density is preferable in this case, as the temperature alleviation is considered low. Consequently, the maximum acceptable current density has been set equal to 3.5 A/mm<sup>2</sup>. This strict constraint sets also a limit to the maximum achievable power density.



The third group concerns physical constraints related to the limited space that the pod structure imposes. For instance, the extended review of the relevant technical literature revealed that the motor's outer diameter ( $D_o$ ) to propeller's diameter ( $D$ ) ratio varies between 0.38 and 0.54. Moreover, its axial length ( $L$ ) should not be higher than 2.60 m when the specific type of vessel is considered. The above-mentioned constraints are essential in order to guarantee the slim and hydrodynamically optimized pod structure. A possible violation of them would significantly reduce the overall propulsion system's efficiency, as the smooth flow of the seawater would not be achievable then. Motors with large axial length and relatively small outer diameter are the most preferable choice. In this case, the specific electric loading ( $a_c$ ), which is inversely proportional to the airgap diameter, increases. If a high power density is required, this quantity should be high. However, too high values for  $a_c$  have negative effects on the temperature rise and the motor's performance. Thus, the upper bound for  $a_c$  has been considered to be equal to 65 kA/m. The fourth group of constraints deals with the mechanical robustness of the motor and its manufacturing feasibility. The stator slots should be large enough to accommodate a large amount of copper and insulation with thickness of 1.22 and 0.5 mm for the slot liner and the slot wedge, respectively. According to the applied voltage level, the insulation specifications of class F have been taken into account. Moreover, it must be geometrically possible for the coils to be placed in the slots. The round copper wires are usually radially inserted through the slot opening. Therefore, the slot opening width ( $b_{ss0}$ ) has to be larger than their diameter. However, a relatively large slot opening width has adverse impact on the cogging torque and the flux leakage. On the contrary, a semiclosed slot configuration benefits the winding's self-inductance and, thus, reduces the short-circuit current.

The rectangular wires can be combined with a smaller slot opening width, since they are axially inserted in the slot. The current technology and several winding techniques enable the easy manufacturing and the proper arrangement of enameled rectangular copper windings with maximum width of 20 mm and maximum thickness of 5.6 mm [25]. A slot fill factor equal to 70% can also be easily achieved when modular motor configurations are used. In addition, according to the international-standard series IEC 317, the maximum current that can pass continuously through a single wire is equal to 302 A. Thus, the use of multistrands coils is necessary.

Another important geometrical constraint refers to the total slot height ( $h_{ss}$ ). Deep slots are preferable when the achievement of high power density is the main priority. However, the deep slots can provoke increased copper losses, overheating, high leakage inductance, low power factor, and high cost for the overall drive system. In [26], it was concluded that for PMSMs, whose specifications are similar to the corresponding ones considered here, the  $h_{ss}$  should not exceed 150 mm. Also, the airgap length ( $\delta$ ), it should not be less than 6 mm for manufacturing reasons and aiming to avoid saturation on the stator teeth. At the same time, the magnets height ( $l_m$ ) should not exceed 25 mm. It is a common practice for designers to increase  $l_m$  in order to avoid irreversible demagnetization,

TABLE II  
MOTOR CHARACTERISTICS AND CONSTRAINTS

Quantity	Symbol	Value/Constraint	Unit
Output power	$P_{out}$	4.054	MW
Output torque	$T_{out}$	193.58	kNm
Nominal speed	$n$	200	rpm
Efficiency	$\eta$	$\geq 95$	%
Power factor	$\cos \phi$	$\geq 0.95$	-
Line to line voltage	$V_L$	525-690	V
Poles number	$2p$	10-90	-
Slot number	$Q_s$	12-108	-
Phase current	$I_{ph}$	$\leq 4.5$	kA
Current density	$J_s$	$\leq 3.5$	A/mm <sup>2</sup>
Turns per phase	$N_s$	$\leq 20$	-
Electric loading	$a_c$	$\leq 65$	kA/m
Slot fill factor	$sf$	$\leq 70$	%
Motor's outer diameter	$D_o$	$0.38D \leq D_o$ $D_o \leq 0.54D$	m
Motor's axial length	$L$	$\leq 2.6$	m
Airgap length	$\delta$	$\geq 6$	mm
Magnets height	$l_m$	$\leq 25$	mm
Stator slot height	$h_{ss}$	$\leq 150$	mm
Slot opening width	$b_{ss0}$	$\geq 6$	mm
Slot width at the top	$b_{ss2}$	$0.15h_{ss} \leq b_{ss2}$ $b_{ss2} \leq 0.80h_{ss}$	mm
Stator yoke height	$h_{sy}$	$h_{sy} \geq h_{ss}/2$	mm
Stator tooth tip height	$h_{sw}$	$\geq 4$	mm
Stator/Rotor core flux density	$B_{sy}, B_{ry}$	$\leq 1.60$	T
Stator teeth flux density	$B_{st}$	$\leq 1.80$	T
Airgap flux density	$B_g$	$\leq 0.90$	T

but the manufacturing complexity and cost also increase. Likewise, numerous constraints related with other geometrical parameters have been taken into account in order to ensure the desirable operation. The design variables range and the adopted constraints are summarized in Table II.

### B. Proposed PMSM Design Methodology

The classical PMSM design procedure starts with the motor's sizing equation, which relates the motor's apparent power ( $S$ ), with the motor's volume. For given winding factor ( $k_w$ ), speed ( $n$ ), electric ( $a_c$ ), and magnetic loading ( $B_{av}$ ), the quantity  $D_s^2 L$  can be derived from the following equation:

$$D_s^2 L = \frac{S}{1.1\pi k_w B_{av} a_c n} \quad (3)$$

Then, the designer has to select the proper ratio of the active motor's length ( $L$ ) to the stator's inner diameter ( $D_s$ ) according to various design criteria. Despite the fact that a large number of research works provides directions about this choice, each one of them benefits only a specific performance feature. However, for a pod propulsion motor, a high efficiency combined with an enhanced fault-tolerance capability and a high power density is required. Thus, it is not clear enough for which ratio the motor will present all the aforementioned characteristics. Although the incorporation of an optimization algorithm could provide a solution to this problem, some of the examined features are conflicting and, consequently, there

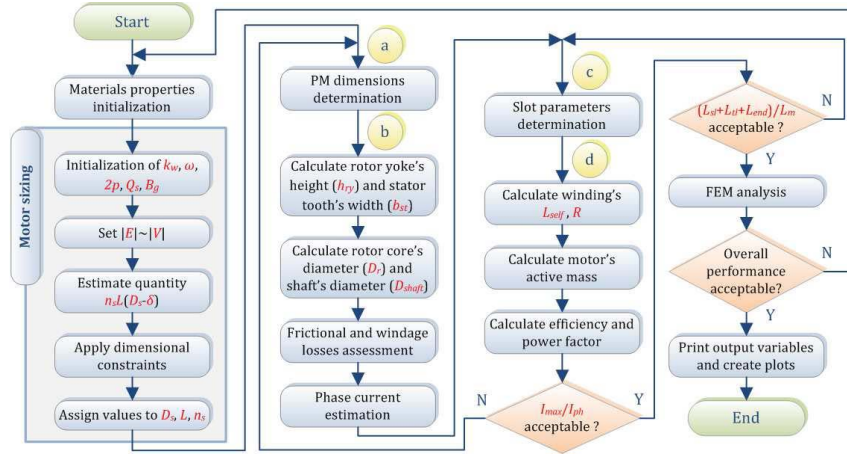


Fig. 10. General scheme of the developed multicriteria PMSM design software tool.

is great risk of missing the overall optima. A thorough investigation regarding the ratio  $D_s/L$  along with a multicriteria design approach can guarantee that all the requirements will be satisfied. At the same time, the mechanisms that limit the power density will be further highlighted.

For this reason, the authors developed an effective PMSM design tool in order to create the motors topologies, validate their performance through finite-element analysis, and assess the obtained results by the appropriate graphical feedback. The developed tool is analytically described in the flowchart depicted in Fig. 10. As it can be seen, it consists of a main routine and several subroutines. The subroutines related with the determination of the basic motor's dimensions, permanent magnets characteristics, and the slot parameters will be discussed in detail as text follows in order to explain some important considerations of the proposed here design methodology. The process starts with the incorporation of the materials properties. A high quality silicon steel with laminations thickness of 0.35 mm has been selected both for stator and rotor core according to the instructions of NEMA and IEC. Moreover, high energy NdFeB magnets with remanent flux density of 1.23 T have been chosen. During the design procedure, the temperature has been set equal to 100 °C. Thus, the materials properties have been appropriately modified. Next, for the determination of  $D_s$  and  $L$ , the authors adopted a different approach (summarized in Fig. 10) compared to the traditional one shown in (3). In this methodology, the amplitude of the induced voltage ( $E$ ) has been set equal to the corresponding one of the applied phase voltage ( $V_{ph}$ ) aiming to limit the phase current ( $I_{ph}$ ) and, consequently, minimize the copper and motor's total mass. A high induced voltage results also to a high power factor, while at the same time, this control method decreases the motor's and inverter's cost according to [26]. Preliminary assumptions have to be established for the airgap flux ( $B_g$ ) and the airgap length ( $\delta$ ). Then, the initialization of the angular frequency ( $\omega$ ), the winding factor ( $k_w$ ), and the number of slots per pole and per phase ( $q$ ) follows for each one of the 32 examined poles/slots combinations. Then, the product of  $n_s(D_s - \delta)L$  can be obtained by applying (4), in which  $n_s$  is the number of conductors per slot. Finally, by incorporating the constraints related with  $L$  and the number of turns per phase

$N_s$  ( $N_s = n_s Q_s / 2m$ ), a large number of possible solutions (i.e., products of  $n_s(D_s - \delta)L$ ) was derived. Their number was equal to 1706 and their management would not be feasible without the utilization of the developed tool.

$$n_s(D_s - \delta)L = \frac{\sqrt{2}E}{\omega k_w q B_g} \quad (4)$$

The calculation of the permanent magnet height ( $l_m$ ) and pole-arc to pole pitch ratio ( $2a$ ) was conducted through a repetitive process [presented in Fig. 11(a)]. The designer has to assign a value to the slot opening width ( $b_{s0}$ ). A small  $b_{s0}$  should be selected as previously described. For the minimization of cogging torque, the values of  $2a$  were obtained from (5), where  $k$  is an integer number that takes consecutively values from 1 to  $(\text{LCM}(Q_s, 2p)/2p) - 1$  with a step of 1 [27]. Starting with the minimum allowable value for  $2a$  and a small value for  $l_m$  the maximum amplitude of the flux density in the airgap ( $B_m$ ) is then estimated by using (6), where  $B_r$  is the remanent flux density,  $\mu_r$  is the magnet relative permeability,  $\delta_e$  is the equivalent airgap length,  $D_r$  is the rotor core diameter, and  $r$  is defined as  $r = D_s/2 - \delta$ . Reader can refer to [28] in order to find more information about the estimation of  $\delta_e$ . The process stops when the value of  $B_m$  is equal to one of  $B_g$ . If the above does not happen, the procedure starts again by assigning to  $2a$  the next available value and using a higher value for  $l_m$ . Thus, this routine guarantees that the minimum permanent magnets mass will be used aiming to improve power density and reduce the cost. Then, the design process continues with the determination of the rotor yoke height ( $h_{ry}$ ), the stator tooth width ( $b_{st}$ ), the rotor core diameter ( $D_r$ ), and the shaft diameter ( $D_{shaft}$ ) as analytically described in [29]. For the calculation of the specific parameters, the maximum allowable values for the stator ( $B_{sy}$ ) and rotor yoke ( $B_{ry}$ ) flux densities (given in Table II) were taken into account.

$$2a = \frac{(\text{LCM}(Q_s, 2p)/2p) - k}{\text{LCM}(Q_s, 2p)/2p} \quad (5)$$

$$B_m(r) = \frac{l_m B_r}{r \left[ \ln \left( \frac{D_r + 2l_m}{D_r} \right) + \mu_r \ln \left( \frac{D_r + 2l_m + 2\delta_e}{D_r + 2l_m} \right) \right]} \quad (6)$$

Next, the estimation of the windage ( $P_{wind}$ ) and frictional losses ( $P_f$ ) is conducted. For the sake of space, reader can



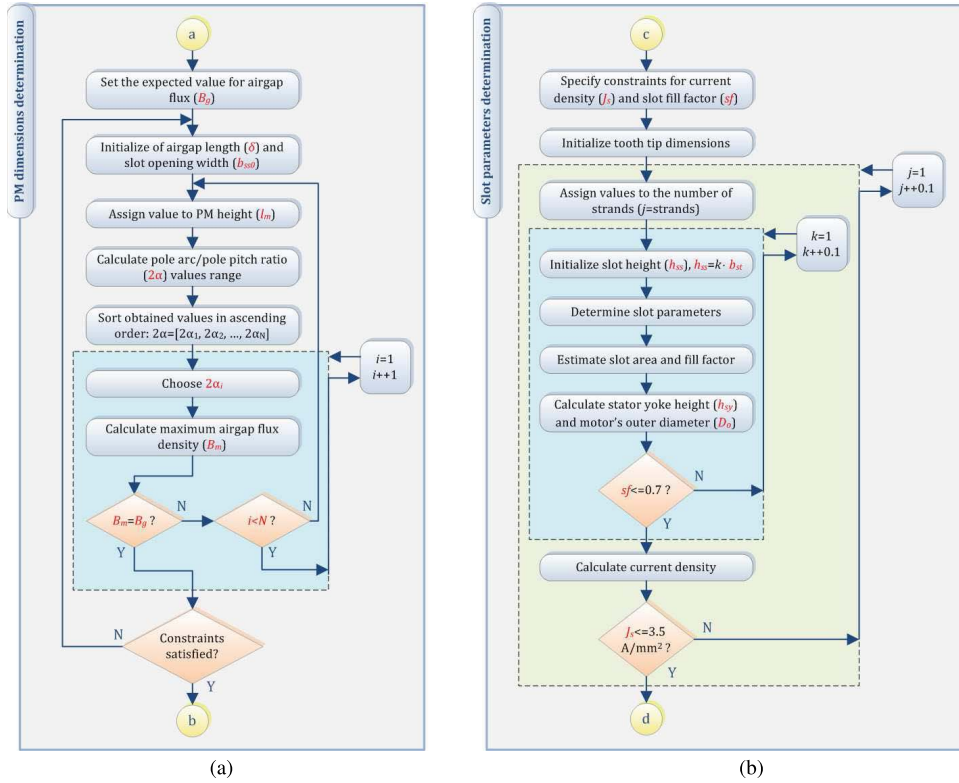


Fig. 11. Detailed view of the subroutines used for the calculation of (a) permanent magnets dimensions and (b) slot geometrical parameters.

refer to [28] for more details. Afterward, for given output power ( $P_{out}$ ), the phase current  $I_{ph}$  is obtained from (7). Another repetitive process [presented in Fig. 11(b)] was incorporated for the calculation of the slot geometrical parameters and the stator winding characteristics. This procedure starts with the initialization of the tooth tip height ( $h_{st}$ ) and next with continuous permutations on: 1) the number of strands per conductors; 2) the wire's cross section; and 3) the slot's total height ( $h_{ss}$ ) tries to find out a slot configuration which accommodates the windings and also satisfies the constraints related with the current density ( $J_s$ ) and the slot fill factor ( $sf$ ). The variable  $h_{ss}$  varies according to the tooth width ( $b_{st}$ ) in order to avoid deep slots and, thus, saturable operation, and too high values for the winding self-inductance and, thus, a low power factor. The rest slot geometrical parameters can be estimated by using the analytical equations provided in [30]

$$I_{ph} = \frac{P_{out} + P_{wind} + P_f}{mE} \quad (7)$$

Then, the calculation of the winding self-inductance ( $L_{self}$ ) and resistance ( $R$ ) follows. Each one of the self-inductance components, such as the synchronous inductance ( $L_m$ ), the slot leakage inductance ( $L_{sl}$ ), the tooth tip leakage inductance ( $L_{tl}$ ), and the end-windings leakage inductance ( $L_{end}$ ) were calculated according to the equations provided in [28] and [29]. For the determination of motor's efficiency except from the copper losses ( $P_{cu}$ ), the iron ( $P_{iron}$ ) and permanent magnets losses ( $P_{pm}$ ) were also considered. The estimation of the aforementioned losses was conducted by incorporating the analytical equations given in [28] and by considering that the flux densities in the core parts are equal to the maximum allowable values given in Table II. Next, after the interaction of

the tool with a commercial software, all the losses types were reestimated through 2-D FEM analysis in order to achieve increased accuracy. In addition, aiming to limit the risk of magnets' demagnetization, the maximum allowable current that the motor can absorb before the demagnetization occurs was derived from (8) [30], where  $B_D$  is the flux density value in which the demagnetization starts. Then, the ratio  $I_{max}/I_{ph}$  is calculated and if its value is not acceptable, the procedure returns to a previous step in order to recalculate the magnets dimensions, as it can be seen from Fig. 10. A last check point follows. Specifically, in order to limit the short-circuit current and, thus, enhance the motor's fault-tolerance capability, the ratio  $(L_{sl} + L_{tl} + L_{end})/L_m$  must be greater than the quantity given in (9) [31]. If this does not happen, the increment of the slot and tooth tip leakage is necessary through the redetermination of the slot geometrical parameters. When a topology satisfies all the applied constraints, FEM analysis is conducted in order to validate the motor's performance. Each topology is analyzed both at no-load and full-load operation and important characteristics, such as the cogging torque and the torque ripple are also specified.

$$I_{max} = \pi 2p \frac{B_r l_m - B_D (l_m + \delta)}{6\mu_0 \mu_r k_w N_s} \quad (8)$$

$$\frac{L_{sl} + L_{tl} + L_{end}}{L_m} \geq \left( \frac{8B_r l_m 2a}{\pi (B_r l_m - B_D \delta_e)} \right) - 1 \quad (9)$$

### C. Important Design Choices and Results

In this paragraph, the authors provide useful directions about the selection of the proper poles/slots combination and  $D_s/L$  ratio. The proposed methodology is implemented in three

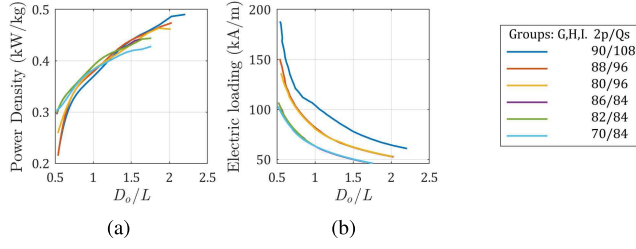


Fig. 12. (a) Power density and (b) electric loading variation as a function of  $D_o/L$  ratio for the motor topologies of Groups G, H, and I.

TABLE III  
POLES/SLOTS COMBINATIONS GROUPS

Group	(2p)	( $Q_s$ )
A	10, 14	12
B	20, 22, 26, 28	24
C	30, 34, 38, 42	36
D	40, 44, 46, 50, 52, 56	48
E	50, 58, 62	60
F	60, 66, 68, 70, 74, 76, 78	72
G	70, 82, 86	84
H	80, 88	96
I	90	108

phases (i.e., phases A–C) and at each step, a discussion is made over the derived results. For the better organization of this context and in order to be easier for the authors to refer to the examined poles/slots combinations, it was decided to separate them in groups A through E. These groups are given in Table III. All the combinations that belong to a specific group have the same number of slots and turns per phase.

1) “Phase A” (*Rejection of Unsuitable Combinations*): Few of the examined combinations should be rejected, as in their case, some of the constraints described in Section IV are violated. This happens for all the combinations that belong to groups G, H, and I. For the specific topologies, the power density variation as a function of the ratio  $D_o/L$  is illustrated in Fig. 12(a). It must be mentioned here that the authors decided to depict the variation of the investigated parameters along with the ratio  $D_o/L$  instead of  $D_s/L$ , since the motor’s outer diameter ( $D_o$ ) is related with important constraints given in Table II. From Fig. 12(a), it can be seen that the power density increases as the value of the ratio becomes higher. The same can also be noted when the poles number becomes greater. The maximum recorded values for the combinations of these groups vary from 0.42 to 0.49 kW/kg. However, the above ratings are achievable only when  $D_o$  is larger than 2.2 m, and thus, the topologies have an outer diameter much larger than their axial length. This feature does not coincide with the characteristics of a typical pod structure. Moreover, the ratio  $D_o/D$  is higher than 0.54 in the specific cases and, consequently, another constraint related to the vessel’s hydrodynamic performance is violated.

Configurations with a lower  $D_o/L$  ratio may be the solution to this problem, as they exhibit power density up to 0.30 kW/kg even for the minimum ratio value. This power density rating is higher than the corresponding one (i.e., 0.23 kW/kg) presented by the already installed pod propulsion motors with the same output power according to the data

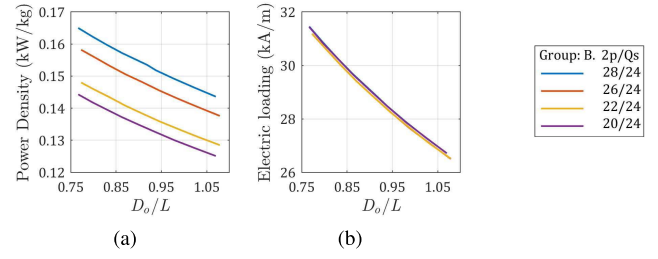


Fig. 13. (a) Power density and (b) electric loading variation as a function of  $D_o/L$  ratio for the motor topologies of Group B.

provided in Fig. 2. However, by inspecting Fig. 12(b), it is observed that the specific electric loading increases significantly as the motor’s diameter decreases. Even for a ratio equal to 1, the electric loading expands from 68 to 103 kA/m, while it varies from 100 to 180 kA/m when the ratio becomes minimum for each combination. In addition, the total slot’s height ( $h_{ss}$ ) was larger than 150 mm for the majority of the topologies, which is not acceptable and also saturation was observed in the stator teeth due to their small width. On the basis of the above, all the configurations derived from groups G through I have been excluded and no further investigated, despite the fact that they present the highest power density ratings among all the examined poles/slots combinations. Group B was the next one that has been rejected. In this case, the electric loading takes allowable values as it can be seen from Fig. 13(b). Nevertheless, the maximum achievable power density was way too low (compared to the value of 0.23 kW/kg) for the all feasible combinations of  $n_s$ ,  $D_s$  and  $L$ . The maximum value (recorded for the combination 28/24) was equal to 0.165 kW/kg. Furthermore, it must be mentioned that the power density (depicted in Fig. 13(a)) follows a different trend, as it decreases with the increment of the ratio  $D_o/L$ . A considerable enhancement is observed for the specific parameter when the poles number increases. Regarding combinations 10/12 and 14/12 (i.e., group A), they failed to fulfill the motor’s torque requirements and were also excluded.

2) “Phase B” (*Investigations on  $D_o/L$  Ratio Effect*): It has been proven so far that 12 of the 32 preliminary proposed poles/slots combinations are not suitable for this application. For the remaining combinations (i.e., groups C, D, E, and F), further investigations were conducted. At this step, the impact of the ratio  $D_o/L$  variation on important motor’s features, such as power density, electric loading, efficiency, power factor, winding’s self-inductance, magnets’ mass, motor’s total mass, and cost, was studied. The obtained results are presented in Fig. 14. Focusing deeper on these results, we address and justify here the main findings for each parameter as follows.

- **Power Density:** Generally, for a given number of slots, when the poles number increases the power density also increases for all the examined groups. On the other hand, this parameter presents a different trend for each group as the ratio  $D_o/L$  increases. Specifically, for group C, it becomes higher as the ratio increases, next acquires its maximum value for ratio value equal to 1 and after this point follows a declining trend. The maximum recorded values for group C vary from 0.29 to 0.33 kW/kg,

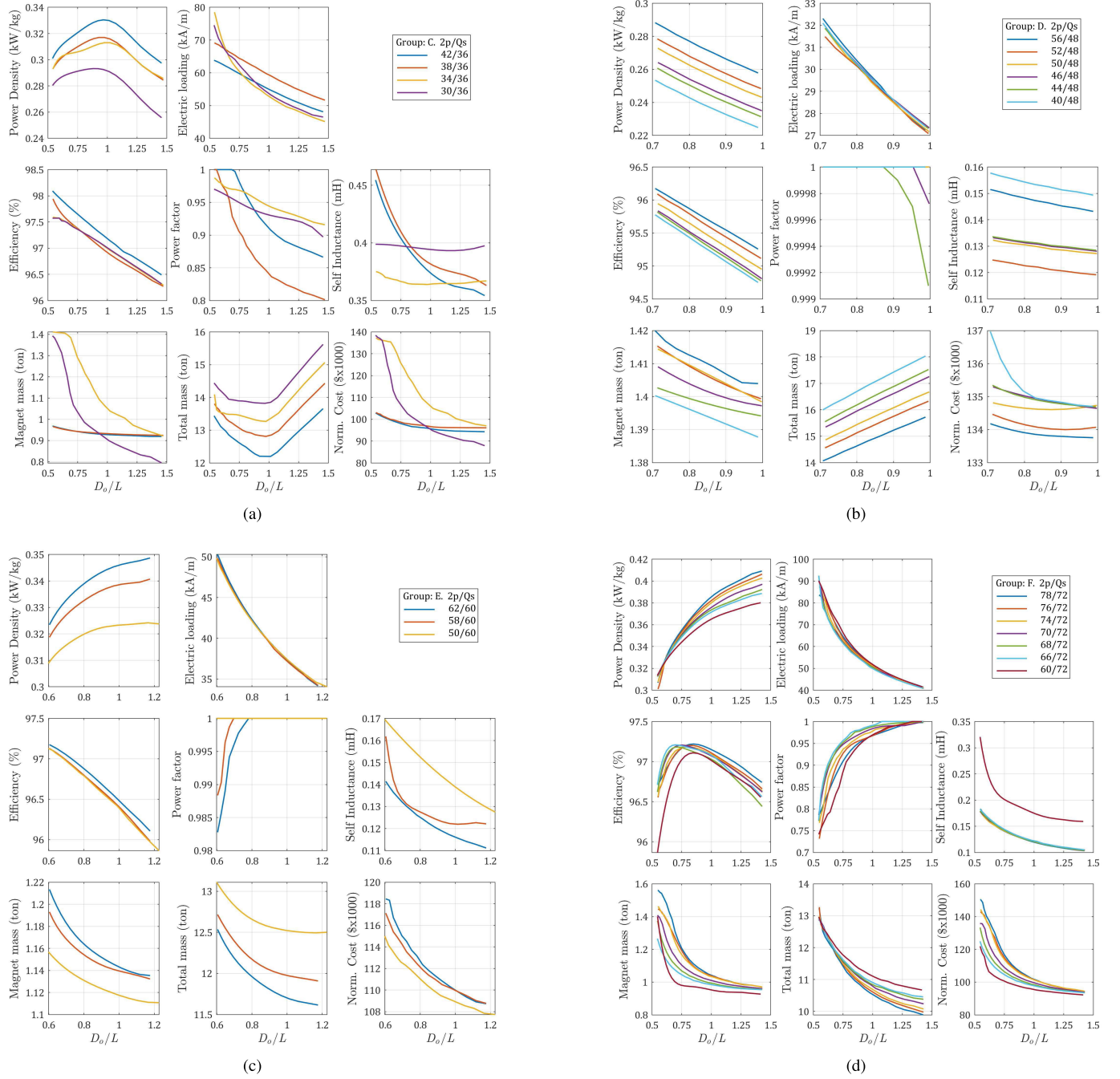


Fig. 14. Motor performance characteristics variation as a function of  $D_o/L$  ratio for the topologies of: (a) Group C, (b) Group D, (c) Group E, and (d) Group F.

while the minimum one is equal to 0.25 kW/kg. Thus, the improvement range for power density (taking the value of 0.23 kW/kg as reference point) expands from 8.69% to 43.47%. The number of turns per phase is equal to 12 for all the topologies of group C.

In the case of group D, the power density decreases as the ratio becomes greater. It gets maximum when the ratios  $D_o/L$  and  $D_s/L$  are equal to 0.71 and 0.85 respectively. Its maximization occurs when the motor's diameter is minimum, which is quite attractive for this application. The maximum values vary from 0.253 to 0.288 kW/kg, and thus, an enhancement up to 25.2% has been achieved. However, this value is lower

than the corresponding one obtained when the topologies of group C were used. This can be justified by the fact that the configurations of this group have 8 turns per phase instead of 16, which is the maximum number of turns that could be used, as in the latter case, they failed to meet motor's torque requirement and they have been excluded. A lower number of turns per phase results to a higher product of  $(D_s - \delta)L$  and, thus, to a lower power density.

For the next two groups (i.e., groups E and F), the power density increases significantly as the ratio becomes greater. For group E, the maximum power density rating varies from 0.324 to 0.348 kW/kg, while



the minimum one is equal to 0.308 kW/kg and is obtained when combination 50/60 is used. In this case, an improvement of about 33.91% can be achieved. When the topology 62/60 is combined with the maximum diameter, the power density can be increased up to 51.3%. Group F yields the highest power density ratings (0.38–0.40 kW/kg) and quite satisfactory values are achievable even when the ratio is lower than 1. In this case, the improvement range expands from 65.21% up to 73.91%. It seems that the combinations of this group benefit significantly this feature. The number of turns per phase for the topologies of groups E and F was 10 and 12, respectively.

- **Electric Loading:** As it was expected a lower value for the ratio  $D_o/L$  results to a higher electric loading. The topologies of groups D and E exhibit a value within the allowable ratings (i.e., lower than 65 kA/m). On the other hand, this constraint is violated for some configurations derived from groups C and F. A quite smaller number of candidate topologies are now available. It seems that the achievement of a low value for this parameter and the minimization of the motor's mass are conflicting features.
- **Efficiency:** A value higher than 94.7% has been achieved for all the investigated topologies. Groups C and E exhibit the highest values, while groups F and D are characterized by slightly lower ones. The efficiency decreases as the ratio  $D_o/L$  becomes greater for all the groups except from group F, where a different trend occurs. Generally, a higher poles number benefits this quantity. Regarding motor's losses, the windage, frictional, and magnet losses increase as the ratio becomes greater. The copper losses are higher than the iron losses for a relatively small poles/slots number. When the poles number increases, the iron losses become dominant. Both of them increase with a larger value for the ratio  $D_o/L$ . A slightly smaller variation has been observed for the iron losses, which seem to be stabilized after a specific ratio value.
- **Power Factor:** When a high power factor is the top priority, groups D and E are the most appropriate choices. Slightly lower values are obtained for groups C and F. In the first case, a small variation is observed as the ratio increases. The pod system requirements are fulfilled only when  $D_o/L$  is lower than 0.75. In the latter case, the specific quantity follows a different trend and a power factor equal at least to 0.95 can be achieved when the ratio is 1.
- **Winding Self-Inductance:** Generally, the self-inductance decreases as the ratio  $D_o/L$  becomes greater. In some cases, small variation occurs and this parameter tends to be stabilized around a specific value. From Fig. 15(b), where the self-inductance components variation is given indicatively for combination 60/72, it is seen that the synchronous inductance ( $L_m$ ) is low and remains almost constant. On the other hand, the leakage inductance ( $L_{leak}$ ) is much higher and follows a declining trend. Thus, topologies with an axial length larger than their outer diameter can be considered as more fault-tolerant,

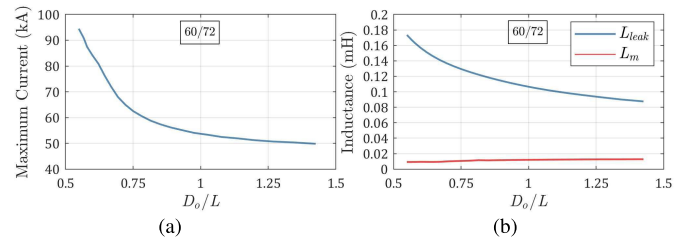


Fig. 15. (a) Maximum allowable current and (b) leakage ( $L_{leak}$ ) and synchronous ( $L_m$ ) inductance variation as a function of  $D_o/L$  for the combination 60/72.

as a higher  $L_{leak}$  can limit the short-circuit current. Moreover, for given slots, a small poles number benefits this quantity. The configurations of group C present the highest values, while the corresponding ones of groups D and E are the lowest ones and these groups should be avoided if motor's fault-tolerance capability is the top priority. Although higher values can be achieved through the reestimation of the slot geometrical parameters, this can lead to power factor's reduction, as these two characteristics are conflicting.

- **Magnets Mass:** As the motor's diameter increases, the permanent magnets mass follows a declining trend. The mass varies slightly along with the ratio, especially for groups D and E. Considerable variation is observed when for the same slots number, a different pole number is used. In the majority of the examined topologies, the magnets mass represents the 10% of the motor's total mass. Thus, the proposed here methodology succeeded to minimize their use. This is quite important from industrial perspective, as the pod propulsion system must reliable and efficient, but also economically feasible.
- **Motor's Total Mass:** Group F provides the lightest motor topologies, while group D the heaviest ones. Considerable variation occurs among combinations with the same slots number, but different poles number. As the poles number increases, the magnetic flux that each pole produces becomes higher, and thus, a larger rotor core height ( $h_{ry}$ ) is needed aiming to avoid saturation. Consequently, groups E and F present a clear advantage. On the contrary, for the topologies derived from groups C and D, the rotor's core mass is increased and, in some cases, is even equal to the stator's core mass.
- **Cost:** For the cost calculation, each material's price is in accordance with the recent economic data collected through search in the international materials market. The cost decreases as the diameter becomes larger than its length. The trend of its curve is strongly related with the corresponding one of the magnet mass, as the magnets are the most expensive component. The topologies of group D present the highest cost. Group F is the most attractive choice when a low cost is desirable.
- **Maximum Allowable Current:** Motor topologies with an axial length larger than their diameter withstand a larger amount of current before the magnets demagnetization occurs. This can be easily concluded by inspecting

TABLE IV  
BASIC DIMENSIONS AND PERFORMANCE CHARACTERISTICS OF THE PROPOSED PMSM TOPOLOGIES

$2p$	$Q_s$	$L$ (m)	$D_s/L$	$D_o/L$	$P_d$ (kW/kg)	$P_d$ increment (%)	$\eta$ (%)	$\cos \phi$	$a_c$ (kA/m)	$I_{max}/I_{ph}$	$L_{self}$ (mH)	Cost (\$x1000)
30	36	2.15	0.628	0.742	0.291	26.52	97.37	0.950	62.74	4.98	0.397	107.24
34	36	1.90	0.812	0.931	0.305	32.61	97.11	0.951	54.70	7.73	0.363	109.46
38	36	2.30	0.554	0.665	0.305	32.61	97.28	0.954	64.95	9.02	0.428	99.93
42	36	2.05	0.690	0.806	0.324	40.87	97.54	0.961	58.63	10.39	0.396	97.16
40	48	2.60	0.644	0.707	0.253	10.00	95.78	1.000	32.10	10.50	0.158	136.96
44	48	2.60	0.649	0.713	0.261	13.48	95.82	1.000	31.86	11.56	0.134	135.34
46	48	2.60	0.650	0.715	0.264	14.78	95.83	1.000	31.89	12.12	0.133	135.29
50	48	2.60	0.650	0.715	0.273	18.70	95.94	1.000	31.85	13.31	0.132	134.78
52	48	2.60	0.649	0.713	0.278	20.87	96.09	1.000	31.28	13.80	0.125	134.46
56	48	2.60	0.644	0.707	0.288	25.22	96.17	1.000	32.30	14.92	0.151	134.17
50	60	2.10	0.789	0.877	0.322	40.00	96.79	1.000	40.17	10.71	0.147	109.95
58	60	2.15	0.762	0.848	0.335	45.65	96.72	1.000	40.80	12.63	0.126	111.38
62	60	2.15	0.762	0.848	0.342	48.70	96.63	1.000	40.91	13.50	0.122	111.82
60	72	1.85	0.848	0.969	0.363	57.83	97.04	0.965	52.96	10.49	0.178	95.96
66	72	1.85	0.855	0.976	0.370	60.87	97.10	0.976	50.65	12.43	0.124	98.15
68	72	1.85	0.856	0.977	0.372	61.74	97.09	0.987	51.22	13.17	0.122	98.75
70	72	1.85	0.857	0.978	0.374	62.61	97.08	0.982	51.31	13.56	0.123	100.10
74	72	1.85	0.857	0.978	0.378	64.35	97.10	0.975	51.79	14.02	0.122	101.97
76	72	1.85	0.856	0.977	0.380	65.22	97.12	0.965	52.08	14.62	0.123	102.13
78	72	1.85	0.855	0.976	0.383	66.52	97.16	0.965	52.55	14.91	0.121	102.38

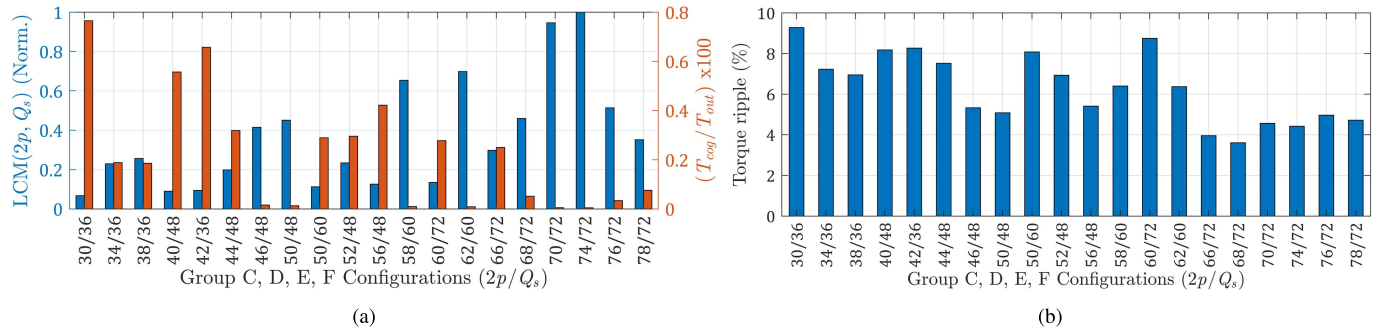


Fig. 16. Characteristics of the proposed PMSM topologies. (a) Normalized  $LCM(2p, Q_s)$  and cogging torque. (b) Torque ripple.

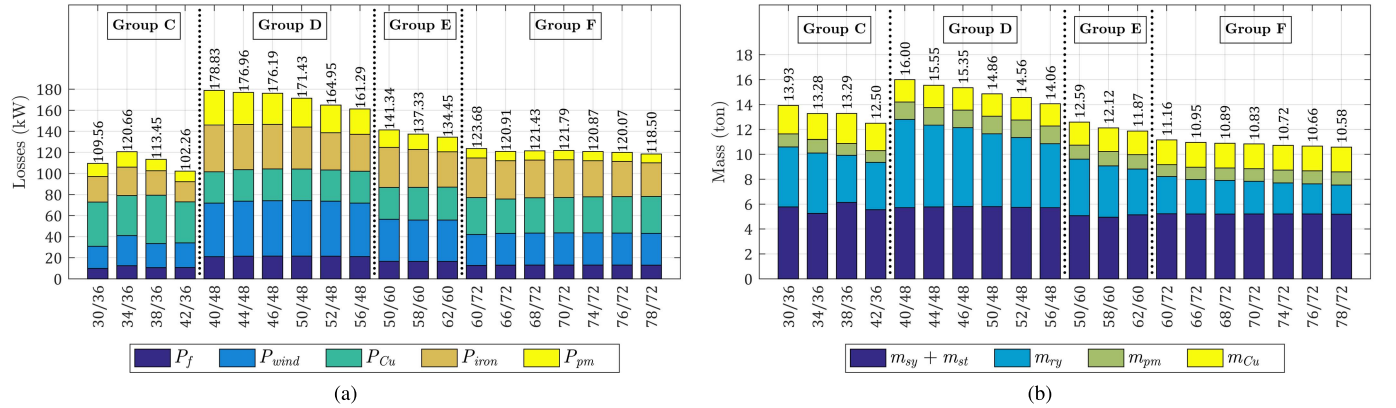


Fig. 17. Cumulative distributions per PMSM group/configuration regarding to: (a) types of losses and (b) different parts' masses.

Fig. 15(a), where the variation of this quantity is given indicatively for the combination 60/72. Also, for given slots number, a higher poles number benefits this feature significantly.

3) “Phase C” (Final Topologies Selection Criteria and Results): The so far presented work revealed that the selection of the proper value for  $D_o/L$  ratio is not an easy task, as many motor's characteristics are conflicting. For instance,

when the specific ratio increases the power density of the topologies of group F becomes greater, while their winding self-inductance decreases. The authors taking into account the already described observations and after the conduction of further investigations propose the implementation of some selection criteria for the determination of the final PMSM topologies. The suggested methodology is organized in the following steps.

*Step 1:* The PMSM configurations that do not meet the main performance constraints (i.e.,  $\cos \phi \geq 0.95$ ,  $\eta \geq 95\%$ , and  $a_c \leq 65$  kA/m) have to be rejected.

*Step 2:* A more strict constraint for the ratio  $D_o/D$  should be applied, as it results to topologies with smaller diameter and more “balanced” performance. Specifically, the value of  $D_o/D$  should not be higher than 0.46 instead of 0.54, which was the value given in Table II. In this case, a compromise between high power density and enhanced fault-tolerance capability can be achieved, while simultaneously all the other requirements are fulfilled.

*Step 3:* Among the remaining configurations for each poles/slots combination, the one with the highest power density should be chosen.

The basic dimensions and important performance characteristics of the final PMSM topologies are given in Table IV. It can be seen that for each group, different values for the  $D_o/L$  and  $D_s/L$  ratios have been derived. For the poles/slots combinations belonging to the same group, both the ratios converge to specific values. The only exception to the aforementioned observation is group C, for which small variation has been recorded. Furthermore, it can be said that the power density and the winding self-inductance of these configurations are slightly or much lower than the corresponding ones that were depicted in Fig. 14. The constraints imposed by this application affect more the two aforementioned quantities than any other characteristic. Their impact is more apparent for groups C and F. However, the power density ( $P_d$ ) of the proposed topologies varies from 0.253 to 0.383 kW/kg. Comparing these values with the power density of already installed motors with the same output power (i.e., 0.23 kW/kg), an increment of 10% up to 66.52% has been achieved. This significant enhancement highlights even more the effectiveness of the proposed here generic multicriteria design methodology, while at the same time reveals that PMSMs with surface-mounted magnets can be considered as an attractive perspective for pod propulsion systems.

## V. FURTHER ANALYSIS, DISCUSSION, AND RECOMMENDATIONS

The implementation of the developed methodology and the deeper analysis of the obtained results provide also directions about other important motor’s features that could be of great use for engineers and designers. For example, the topologies of groups D and E exhibit clear advantage regarding the power factor, but they are characterized by the highest cost. Moreover, if it is desirable to develop a motor with a diameter as small as possible, the selection should be made among the configurations of group C. The motor’s mass and cost minimization is met for the PMSMs of group F. Concerning the ratio  $I_{max}/I_{ph}$ , in the most cases, it varies from 9.02 to 14.92. Thus, a great amount of current must be absorbed before the permanent magnets demagnetization occurs and, consequently, an enhanced overload capability can be achieved. However, for combinations 30/36 and 34/36, the values of the specific ratio can be considered relatively low and these topologies should be avoided. Furthermore, the low values for the electric loading

and a current density lower than 3.5 A/mm<sup>2</sup> for all the derived configurations are adequate indicators about the acceptable motor’s temperature behavior. The incorporation of thermal analysis in the overall presented, here, design methodology seems not to be necessary. Also, the peak-to-peak cogging torque ( $T_{cog}$ ) as a percentage of the motor’s rated torque ( $T_{out}$ ) and the torque ripple of the derived PMSMs are illustrated in Fig. 16. At the same figure, the common multiple (LCM) of  $2p$  and  $Q_s$  is given too. The LCM is normalized using as base the maximum calculated value, which is equal to 2664. This was necessary in order to fit the values into the same plot. It can be seen that the cogging torque is lower than 0.8% of the motor’s nominal torque. The torque ripple estimated under full load operation can be considered low, as it varies from 4% to 9%. These values are quite satisfactory taking into account that fractional PMSMs with semiclosed structures and single layer winding have been used. Although a double layer winding with an open slot configuration may lead to lower values for this quantity, the specific choice cannot satisfy the requirements of this application. The topologies 30/36 and 60/72 present the highest torque ripple and they should be avoided. Cumulative distributions for each design regarding to the losses types and different motor’s parts’ masses are shown in Fig. 17. The topologies of groups F and D exhibit the lowest and the highest magnet losses, respectively.

## VI. CONCLUSION

This paper presented and described a multicriteria design approach for low-speed PMSMs with surface-mounted magnets, which are going to be used in pod propulsion systems. The proposed methodology focuses on the enhancement of motor’s fault tolerance capability and the maximization of its power density. For this reason, several poles/slots combinations were examined and a selection strategy has been developed aiming to find out which configurations improve the aforementioned characteristics. Furthermore, a different approach for the determination of the motor’s airgap diameter and its axial length has been adopted. By developing and using an effective software tool, a large amount of topologies were created and the impact of the motor’s basic dimensions on various motor’s characteristics (e.g., efficiency, power factor, winding’s self-inductance, cost, and magnets mass) was investigated. The relevant results were presented and commented thoroughly. Several strict constraints that are imposed by the specific application were also explained and implemented in order to guarantee that the derived topologies are acceptable from an industrial perspective. Through the postprocessing analysis, useful observations were made and some directions were provided that could be considered helpful and as the starting point for engineers, designers, and pod propulsion motors manufacturers. Finally, it was shown that the specific motor type can present all the desirable characteristics and seems to be an attractive choice for this kind of application.

## REFERENCES

- [1] J. L. Kirtley, A. Banerjee, and S. Englebreton, “Motors for ship propulsion,” *Proc. IEEE*, vol. 103, no. 12, pp. 2320–2332, Dec. 2015. doi: 10.1109/jproc.2015.2487044.



- [2] T. J. McCoy, "Electric ships past, present, and future [technology leaders]," *IEEE Electr. Mag.*, vol. 3, no. 2, pp. 4–11, Jun. 2015. doi: [10.1109/mele.2015.2414291](https://doi.org/10.1109/mele.2015.2414291).
- [3] G. Sulligoi, A. Vicenzutti, and R. Menis, "All-electric ship design: From electrical propulsion to integrated electrical and electronic power systems," *IEEE Trans. Transp. Electrification*, vol. 2, no. 4, pp. 507–521, Dec. 2016. doi: [10.1109/tte.2016.2598078](https://doi.org/10.1109/tte.2016.2598078).
- [4] N. Doerry, J. Amy, and C. Krolick, "History and the status of electric ship propulsion, integrated power systems, and future trends in the U.S. Navy," *Proc. IEEE*, vol. 103, no. 12, pp. 2243–2251, Dec. 2015. doi: [10.1109/jproc.2015.2494159](https://doi.org/10.1109/jproc.2015.2494159).
- [5] A. S. Nanoty and A. R. Chudasama, "Design of multiphase induction motor for electric ship propulsion," in *Proc. IEEE Electr. Ship Technol. Symp.*, Alexandria, VA, USA, Apr. 2011, pp. 283–287. doi: [10.1109/ests.2011.5770882](https://doi.org/10.1109/ests.2011.5770882).
- [6] Y.-U. Cho, S.-L. Lee, G.-H. Kang, and B.-W. Kim, "Design and verification of 200kW interior permanent magnet synchronous motor for ship propulsion," in *Proc. IEEE Conf. Electromagn. Field Comput.*, Miami, FL, USA, Nov. 2016, pp. 1–2. doi: [10.1109/cefc.2016.7816262](https://doi.org/10.1109/cefc.2016.7816262).
- [7] T. Yanamoto, M. Izumi, K. Umemoto, T. Oryu, Y. Murase, and M. Kawamura, "Load test of 3-MW HTS motor for ship propulsion," *IEEE Trans. Appl. Supercond.*, vol. 27, no. 8, Dec. 2017, Art. no. 5204305. doi: [10.1109/tasc.2017.2754270](https://doi.org/10.1109/tasc.2017.2754270).
- [8] S.-H. Lee, J.-P. Hong, J.-K. Kwon, Y.-S. Jo, and S.-K. Baik, "Study on homopolar superconductivity synchronous motors for ship propulsion applications," *IEEE Trans. Appl. Supercond.*, vol. 18, no. 2, pp. 717–720, Jun. 2008. doi: [10.1109/tasc.2008.921334](https://doi.org/10.1109/tasc.2008.921334).
- [9] H. Karmaker, D. Sarandria, M. T. Ho, J. Feng, D. Kulkarni, and G. Rupertus, "High-power dense electric propulsion motor," *IEEE Trans. Ind. Appl.*, vol. 51, no. 2, pp. 1341–1347, Mar./Apr. 2015. doi: [10.1109/tia.2014.2352257](https://doi.org/10.1109/tia.2014.2352257).
- [10] M. Barcaro, N. Bianchi, and S. Bolognani, "Hybrid electric propulsion system using submersed SPM machine," in *Proc. 18th Int. Conf. Elect. Mach.*, Vilamoura, Portugal, Sep. 2008, pp. 1–6. doi: [10.1109/icel-mach.2008.4800089](https://doi.org/10.1109/icel-mach.2008.4800089).
- [11] N. Bianchi, S. Bolognani, and B. Ruzojcic, "Design of a 1000 HP permanent magnet synchronous motor for ship propulsion," in *Proc. 13th Eur. Conf. Power Electron. Appl.*, Barcelona, Spain, Sep. 2009, pp. 1–8.
- [12] F. Caricchi, F. Crescimbeni, and O. Honrati, "Modular axial-flux permanent-magnet motor for ship propulsion drives," *IEEE Trans. Energy Convers.*, vol. 14, no. 3, pp. 673–679, Sep. 1999. doi: [10.1109/60.790934](https://doi.org/10.1109/60.790934).
- [13] G. Patterson, T. Koseki, Y. Aoyama, and K. Sako, "Simple modeling and prototype experiments for a new high-thrust low-speed permanent-magnet disk motor," *IEEE Trans. Ind. Appl.*, vol. 47, no. 1, pp. 65–71, Jan./Feb. 2011. doi: [10.1109/icems.2009.5382888](https://doi.org/10.1109/icems.2009.5382888).
- [14] S.-K. Lee, G.-H. Kang, and J. Hur, "Finite element computation of magnetic vibration sources in 100 kW two fractional-slot interior permanent magnet machines for ship," *IEEE Trans. Magn.*, vol. 48, no. 2, pp. 867–870, Jan. 2012. doi: [10.1109/tmag.2011.2176323](https://doi.org/10.1109/tmag.2011.2176323).
- [15] A. G. Sarigiannidis *et al.*, "Design of surface PM motors for pod application utilizing a 3D hydrodynamic model," in *Proc. 22nd Int. Conf. Elect. Mach.*, Lausanne, Switzerland, Sep. 2016, pp. 2934–2940. doi: [10.1109/icelmach.2016.7732941](https://doi.org/10.1109/icelmach.2016.7732941).
- [16] M. Qiao, C. Jiang, Y. Zhu, and G. Li, "Research on design method and electromagnetic vibration of six-phase fractional-slot concentrated-winding PM motor suitable for ship propulsion," *IEEE Access*, vol. 4, pp. 8535–8543, 2016. doi: [10.1109/access.2016.2636341](https://doi.org/10.1109/access.2016.2636341).
- [17] R. J. Thome, E. Bowles, and M. Reed, "Integration of electromagnetic technologies into shipboard applications," *IEEE Trans. Appl. Supercond.*, vol. 16, no. 2, pp. 1074–1079, Jun. 2006.
- [18] S.-Y. Kim, Y.-D. Yoon, and S.-K. Sul, "Suppression of thrust loss for the maximum thrust operation in the electric propulsion ship," *IEEE Trans. Ind. Appl.*, vol. 45, no. 2, pp. 756–762, Mar./Apr. 2009.
- [19] B. Epps, "On the rotor lifting line wake model," *J. Ship Prod. Des.*, vol. 33, no. 1, pp. 31–45, Feb. 2017. doi: [10.5957/jsp.33.1.150035](https://doi.org/10.5957/jsp.33.1.150035).
- [20] Y. Wang, W. Xuhui, S. Xue, T. Fan, and Z. Lili, "Analysis and design of high power factor interior permanent magnet motor with concentrated windings for undersea vehicle propulsion," in *Proc. IEEE Vehicle Power Propuls. Conf.*, Sep. 2008, pp. 1–6. doi: [10.1109/vppc.2008.4677430](https://doi.org/10.1109/vppc.2008.4677430).
- [21] Z. Liu, J. Wu, and L. Hao, "Coordinated and fault-tolerant control of tandem 15-phase induction motors in ship propulsion system," *IET Electr. Power Appl.*, vol. 12, no. 1, pp. 91–97, Jan. 2018. doi: [10.1049/iet-epa.2017.0274](https://doi.org/10.1049/iet-epa.2017.0274).
- [22] J. Wang, Z. P. Xia, and D. Howe, "Three-phase modular permanent magnet brushless machine for torque boosting on a downsized ICE vehicle," *IEEE Trans. Veh. Technol.*, vol. 54, no. 3, pp. 809–816, May 2005.
- [23] F. Meir, "Permanent-magnet synchronous machines with non-overlapping concentrated windings for low-speed direct-drive application," Ph.D. dissertation, Royal Inst. Technol., School Elect. Eng., Elect. Mach. Power Electron., Stockholm, Sweden, 2008.
- [24] N. Bianchi, S. Bolognani, and M. D. Pre, "Magnetic loading of fractional-slot three-phase PM motors with nonoverlapped coils," *IEEE Trans. Ind. Appl.*, vol. 44, no. 5, pp. 1513–1521, Sep./Oct. 2008. doi: [10.1109/ias.2006.256517](https://doi.org/10.1109/ias.2006.256517).
- [25] J.-H. Choi *et al.*, "Design of high power permanent magnet motor with segment rectangular copper wire and closed slot opening on electric vehicles," *IEEE Trans. Magn.*, vol. 46, no. 6, pp. 2070–2073, Jun. 2010.
- [26] A. Grauers and P. Kasinathan, "Force density limits in low-speed PM machines due to temperature and reactance," *IEEE Trans. Energy Convers.*, vol. 19, no. 3, pp. 518–525, Sep. 2004.
- [27] L. Zhu, S. Z. Jiang, Z. Q. Zhu, and C. C. Chan, "Analytical methods for minimizing cogging torque in permanent-magnet machines," *IEEE Trans. Magn.*, vol. 45, no. 4, pp. 2023–2031, Apr. 2009.
- [28] J. Pyrhonen, T. Jokinen, and V. Hrabovcova, *Design of Rotating Electrical Machines*, 2nd ed. Hoboken, NJ, USA: Wiley, 2009.
- [29] Y. L. Karnavas, I. D. Chasiotis, C. K. Korkas, and S. K. Amoutzidis, "Modelling and multiobjective optimization analysis of a permanent magnet synchronous motor design," *Int. J. Numer. Model., Electron. Netw., Devices Fields*, vol. 30, no. 6, p. e2232, 2017. doi: [10.1002/jnm.2232](https://doi.org/10.1002/jnm.2232).
- [30] T. A. Lipo, *Introduction to AC Machine Design*, 2nd ed. Hoboken, NJ, USA: Wiley, 2004.
- [31] T. Sebastian and G. Slemon, "Transient torque and short circuit capabilities of variable speed permanent magnet motors," *IEEE Trans. Magn.*, vol. 23, no. 5, pp. 3619–3621, Sep. 1987.



**Ioannis D. Chasiotis** (S'13) was born in Athens, Greece, in 1991. He received the Diploma Degree from the Department of Electrical and Computer Engineering, Democritus University of Thrace, Xanthi, Greece, where he is currently pursuing the Ph.D. degree with the Electrical Machines Laboratory.

His current research interests include electrical machines design, the incorporation of AI methods in the design process, and the development of permanent magnet synchronous and induction machines with characteristics of high power density and high efficiency.

Mr. Chasiotis is a member of Hellenic Technical Chamber. He was a recipient of the Full Time Award Scholarship from Onassis Foundation for his Post-Graduate Studies.



**Yannis L. Karnavas** (M'98) was born in Volos, Greece, in 1969. He received the Diploma and Ph.D. degrees from the Department of Electrical and Computer Engineering (DECE), Democritus University of Thrace (DUTH), Xanthi, Greece, in 1994 and 2002, respectively.

From 2004 to 2013, he was the Director of the Electrical Machines and Electrical Installations Laboratories, Department of Electrical Engineering, Technological Educational Institute of Crete, Heraklion, Greece. Since 2013, he has been with the Electrical Machines Laboratory, DECE, DUTH. He has authored or co-authored several papers in various international journals and conferences as well as book chapters in international engineering books. He has participated in many research projects as research leader or scientific associate. His current research interests include electrical machines design, analysis, modeling and optimization, controller design and application to electrical machines, and artificial intelligence methods application to the above areas.

Dr. Karnavas is a Chartered Electrical Engineer and a member of Hellenic Technical Chamber. He is also a member of PES, IAS, and IES. He serves as an Associate Editor and an Editorial Board Member for various international scientific journals.